

Numerical study of cross-polarized plasmons in doped carbon nanotubes

Seiji Uryu*

Department of Physical Science and Materials Engineering, Iwate University, 4-3-5 Ueda, Morioka, Iwate 020-8551, Japan



(Received 4 November 2017; revised manuscript received 23 January 2018; published 19 March 2018)

Excited states in doped carbon nanotubes are numerically studied in an effective-mass approximation and the random-phase approximation. For both metallic and semiconducting nanotubes, plasmons excited by light polarized perpendicular to the nanotube axis appear in a high doping region where the Fermi energy reaches the second lowest conduction band or the second highest valence band, while in no and lower doping regions, they do not exist. The appearance of the plasmons is related to the disappearance of excitons, bound states of electrons and holes. The excitation energy of the plasmons depends on the Fermi energy, which is typically of the order of one electron volt. Our results are in good agreement with recent experimental results.

DOI: [10.1103/PhysRevB.97.125420](https://doi.org/10.1103/PhysRevB.97.125420)

I. INTRODUCTION

Energy dispersion relations of plasmons in one and two dimensions are gapless because divergent behavior of the Coulomb interaction in the long-wavelength limit is weaker than that in three dimensions [1,2]. Thus, as the norm of the wave vector decreases near zero, the excitation energy of the plasmons decreases. In recent years, these plasmons have been intensively studied in metal nanowires [3–8] and graphene [9–15]. Nagao *et al.* observed plasmons in Au-induced one-dimension chains on Si(111) surfaces with electron-energy-loss spectroscopy and showed that the energy dispersion relations of the plasmons are consistent with a theory of plasmons in one dimension, where the excitation energy of the plasmons is about 100 millielectron volts for the wave number of about 0.2 nm^{-1} [3]. Wunsch *et al.* performed similar experiments for graphene, where the energy of plasmons is about 100 millielectron volts for the wave number of about 0.5 nm^{-1} [9]. For carbon nanotubes, plasmons have been reported in many studies as will be mentioned below.

The dependence of the optical absorption spectra of carbon nanotubes on the polarization of light was theoretically shown by Ajiki and Ando [16,17]. For light polarized parallel to the nanotube axis, the wave vector of the light is perpendicular to the nanotube axis and the electric field on the nanotube surface is homogeneous and along the nanotube-axis direction. Thus, electronic states with zero wave vector are excited. For cross-polarized light, which is light polarized perpendicular to the nanotube axis, the wave vector of the light is perpendicular or parallel to the nanotube axis. The electric field projected onto the nanotube surface is along the circumference direction and has the wave vectors in the circumference direction, whose component in this direction is $\pm 2\pi/L$, with L being the circumference length, since the wave vector of light in which we are interested is negligibly small as compared to those of electrons. Thus, electronic states with the wave vectors whose components are about zero and $\pm 2\pi/L$ in the nanotube-axis

and circumference directions, respectively, are excited. In this case, strong depolarization effects suppress the optical absorption. Excitation of excitons can be understood in this theory [18–20]. As mentioned above, external light does not cause purely transverse electromagnetic waves on carbon-nanotube surfaces due to the cylinder shape. Thus, plasmons in nanotubes can be excited by light with parallel polarization and that with cross polarization, where finite nanotube length is needed for the former, although plasmons are longitudinal waves.

Many experimental [21–27] and theoretical [28–33] studies have reported plasmons in carbon nanotubes, whose typical energy is of the order of 10 millielectron volts. Akima *et al.* observed peak structure at about 10 millielectron volts for aligned nanotubes in polymers in optical absorption spectroscopy [22]. They indicated that the peaks can arise from plasmons because the insensitivity of the peaks to carrier doping excludes the other possible origin, narrow energy gap of metallic nanotubes [34–40], which is beyond the scope of this paper and we do not describe in detail. Nakanishi and Ando theoretically studied plasmons in finite-length metallic nanotubes with edges, where the effect of charges induced at the edges is self-consistently calculated with the classical electromagnetic theory [30]. They showed that plasmons with the wave vector π/A in the nanotube-axis direction, where A is the nanotube length, mainly contribute to the optical absorption spectra, and the effect of the edges is negligible because electric fields caused by the charges at the edges are screened to rapidly decay inside the nanotubes. They also showed that the excitation energy of the plasmons in nanotubes almost linearly depends on the wave vector in the long-wavelength limit because of the weak logarithmic dependence of the Coulomb interaction on the wave vector [30].

It has been known that in the optical absorption spectra of doped carbon nanotubes, peaks different from those originating from the above-mentioned plasmons appear [41,42]. Recently, Igarashi *et al.* indicated that these peaks come from plasmons excited by cross-polarized light, which we call the cross-polarized plasmons [43]. The result has two features: one is that the plasmons appear only for high doping levels where the

*uryu@iwate-u.ac.jp

Fermi energy reaches the second lowest conduction band or the second highest valence band; the other is that the excitation energy of the plasmons is around one electron volt. For the latter, Wei and Wang calculated energy dispersion relations of plasmons with finite wave vectors in the circumference direction by using the classical electrodynamic theory and electronic excitations calculated with the hydrodynamic theory, which show that the excitation energies of the plasmons are finite [32]. Sasaki *et al.* reported a numerical value of the excitation energy of the cross-polarized plasmons, which is consistent with the experimental one, by calculations with the classical electromagnetic theory and the Drude conductivity [33]. On the other hand, the former feature still remains unclarified.

The excitation energies of about one electron volt for the cross-polarized plasmons are in a frequency range from infrared to visible, where excitons, bound states of electrons and holes, appear in semiconducting and metallic carbon nanotubes [18,19,44–53]. Excitons play important roles in the optical properties of carbon nanotubes because they cause peaks with large intensity in the optical absorption and photoluminescence spectra [18,19,44–47,49,50] and have been used to identify the chiralities of nanotubes [50]. In the experiments of the cross-polarized plasmons, the doping-level dependence of the optical absorption spectra showed that the appearance of the cross-polarized plasmons follows the disappearance of the excitons excited by light polarized parallel to the nanotube axis [43]. This suggests that comparative studies of the plasmons and excitons are necessary to analyze the experimental results.

The purpose of this study is to numerically clarify the cross-polarized plasmons. To this end, we use the random-phase approximation (RPA) for calculations of excited states based on one-particle states in an effective-mass approximation. The RPA enables simultaneous calculations of plasmons and excitons. In fact, plasmons and excitonic states in graphene are well described with this method [54].

The paper is organized as follows: In Sec. II, an effective-mass approximation and the RPA are presented to describe one-particle electronic states and many-body excited states, respectively, in carbon nanotubes. A formulation of optical absorption spectra is also mentioned. In Sec. III, numerical results in the lowest-order effective-mass approximation are shown to clarify the fundamental properties of the cross-polarized plasmons. In Sec. IV, results calculated in the effective-mass approximation with higher-order corrections are quantitatively compared with the experimental results. A summary and conclusions are mentioned in Sec. V.

II. MODEL AND METHOD

A. Effective-mass approximation

In carbon nanotubes, electronic states near the Fermi energy are described in an effective-mass approximation. For each of two valleys, K and K' points, electronic states are described by a $\mathbf{k} \cdot \mathbf{p}$ equation $H\mathbf{F}(\mathbf{r}) = \varepsilon\mathbf{F}(\mathbf{r})$ [55,56], where H is a Hamiltonian matrix, $\mathbf{F}(\mathbf{r})$ is an envelope function at position $\mathbf{r} = (x, y)$ with x and y being the coordinates in the circumference and nanotube-axis directions, respectively, and ε is an eigenenergy.

For the K point, the Hamiltonian is given by [55–59]

$$H^K = \begin{pmatrix} \sqrt{3}a\gamma S\hat{\mathbf{k}}^2/2 & h(\hat{\mathbf{k}}) \\ h^\dagger(\hat{\mathbf{k}}) & \sqrt{3}a\gamma S\hat{\mathbf{k}}^2/2 \end{pmatrix}, \quad (1)$$

where γ is a band parameter, $\hat{\mathbf{k}} = (\hat{k}_x, \hat{k}_y) \equiv -i\vec{\nabla}$, a is the lattice constant, $h(\hat{\mathbf{k}}) = \gamma(\hat{k}_x - i\hat{k}_y) + (\beta a\gamma/4\sqrt{3})e^{3i\eta}(\hat{k}_x + i\hat{k}_y)^2$ with η being a chiral angle, β and S are dimensionless parameters characterizing the trigonal warping of energy bands and the electron-hole (e-h) asymmetry, respectively, and the energy origin is set at the Fermi energy for no doping.

A boundary condition in the circumference direction for the K point is $\mathbf{F}(\mathbf{r} + \mathbf{L}) = \mathbf{F}(\mathbf{r}) \exp[2\pi i(\varphi - \nu/3)]$ [56,58] with \mathbf{L} being the chiral vector, $\nu = 0$ for metallic nanotubes and ± 1 for semiconducting nanotubes, and φ being an effective magnetic flux threading the nanotube cross section due to the curvature and lattice distortion. The phase is given by $\varphi = -(2\pi/4\sqrt{3})(a/L)p \cos 3\eta$ [60–65], where p is a dimensionless parameter.

An eigenfunction for a state, which we denote as t , is a plain wave $\mathbf{F}(\mathbf{r}) = \mathbf{F}_t e^{i\kappa_t x + ik_t y} / \sqrt{AL}$, with κ_t and k_t being the components of the wave vector in the circumference and nanotube-axis directions, respectively, where $\kappa_t = (2\pi/L)(n + \varphi - \nu/3)$ with n being a band index. The vector \mathbf{F}_t and the eigenenergy ε_t are given by [59]

$$\mathbf{F}_t = \frac{1}{\sqrt{2}} \begin{pmatrix} \frac{h(\mathbf{p}_t)}{|h(\mathbf{p}_t)|} \\ s_t \end{pmatrix}, \quad \varepsilon_t = s_t |h(\mathbf{p}_t)| + \frac{\sqrt{3}a\gamma S}{2} \mathbf{p}_t^2, \quad (2)$$

with $\mathbf{p}_t = (\kappa_t, k_t)$ and $s_t = \{\pm 1\}$, where $+1$ and -1 indicate the conduction and valence bands, respectively. States for the K' point are similarly obtained. Therefore, the one-particle state is characterized by (v_t, s_t, \mathbf{p}_t) with $v_t = \{K, K'\}$.

In the lowest-order approximation with $\beta = S = p = 0$, we have for the state denoted by t for the K point [56]

$$\mathbf{F}_t = \frac{1}{\sqrt{2}} \begin{pmatrix} \frac{\kappa_t - ik_t}{\sqrt{\kappa_t^2 + k_t^2}} \\ s_t \end{pmatrix}, \quad \varepsilon_t = s_t \gamma \sqrt{\kappa_t^2 + k_t^2}, \quad (3)$$

with $\kappa_t = (2\pi/L)(n - \nu/3)$. In this case, the e-h symmetry exists. In metallic nanotubes with $\nu = 0$, energy bands with indices $\pm n$ are degenerate. The bottoms of the degenerate second lowest conduction bands with $n = \pm 1$ are located at $\varepsilon_t(2\pi\gamma/L)^{-1} = 1$. In semiconducting nanotubes, the bottoms of the lowest ($n = 0$) and second lowest ($n = 1$ for $\nu = 1$ and -1 for $\nu = -1$) conduction bands are located at $\varepsilon_t(2\pi\gamma/L)^{-1} = \frac{1}{3}$ and $\frac{2}{3}$, respectively. Because of the e-h symmetry, the energies at the tops of the valence bands are given by the energies at the conduction-band bottoms with the same band indices where the signs of the energies are reversed. The energy bands for the K' point are given by those for the K point where the signs of the band indices are changed.

The Hamiltonian with the Coulomb interaction is written as

$$\mathcal{H} = \sum_t \varepsilon_t c_t^\dagger c_t + \frac{1}{4} \sum_{r,s,t,u} \bar{v}_{rstu} c_r^\dagger c_s^\dagger c_u c_t, \quad (4)$$

where r, s, t , and u specify one-particle states, c_r is an annihilation operator of a state r , and c_s, c_t , and c_u are similarly defined. The matrix elements of the Coulomb interaction are

given by $\bar{v}_{rstu} = v_{(r;t)(s;u)} - v_{(r;u)(s;t)}$, where [18]

$$v_{(r;t)(s;u)} = \delta_{v_r, v_t} \delta_{v_s, v_u} \delta_{\mathbf{p}_r - \mathbf{p}_t, \mathbf{p}_u - \mathbf{p}_s} \frac{2e^2}{\kappa A} \times I_{|\Delta|} \left(\frac{L|k_r - k_t|}{2\pi} \right) K_{|\Delta|} \left(\frac{L|k_r - k_t|}{2\pi} \right) \times (\mathbf{F}_r^\dagger \mathbf{F}_t) (\mathbf{F}_s^\dagger \mathbf{F}_u), \quad (5)$$

with e being the elementary charge, κ being a dielectric constant resulting from the surrounding environment and electrons far away from the Fermi energy, $\Delta = (2\pi/L)^{-1}(\kappa_r - \kappa_t)$, and $I_m(z)$ and $K_m(z)$ being the modified Bessel functions of the first and second kind, respectively. The factor $\frac{1}{4}$ instead of $\frac{1}{2}$ on the right-hand side of Eq. (4) comes from the antisymmetrization of the matrix elements of the Coulomb interaction.

According to earlier studies [19,59,66,67], we use the parameters in numerical calculations $\gamma = 5.8$ eVÅ, $\beta = 1.5$, $p = -0.2$, and $S = 0.2$. For a nanotube with a typical diameter of 1.4 nm, a typical kinetic energy is $2\pi\gamma/L \approx 0.8$ eV. The dimensionless parameter of the Coulomb interaction is chosen as $e^2/2\pi\kappa\gamma = 0.15$ ($\kappa \approx 2.4$) [19,66], which is at most ~ 0.35 for $\kappa = 1$, unless otherwise specified. The parameter γ is related to a resonance integral $-\gamma_0$ for nearest-neighbor π orbitals in a tight-binding model through $\gamma = \sqrt{3}\gamma_0 a/2$ [56,58] leading to $\gamma_0 \approx 2.7$ eV.

B. Random-phase approximation

We consider excited states given by $|\nu\rangle = Q_\nu^\dagger |G\rangle$, where $|G\rangle$ is the ground state and Q_ν^\dagger denotes creation operators for the excited states. The ground state is defined as the state satisfying $Q_\nu |G\rangle = 0$ for all Q_ν . The RPA equation is derived from the equation of motion for Q_ν^\dagger as follows [68,69]. From the equation $\mathcal{H}Q_\nu^\dagger |G\rangle = E_\nu Q_\nu^\dagger |G\rangle$ with E_ν being the eigenenergy of the excited states, we have the equation

$$[\mathcal{H}, Q_\nu^\dagger] |G\rangle = \hbar\Omega_\nu Q_\nu^\dagger |G\rangle, \quad (6)$$

where $\hbar\Omega_\nu = E_\nu - E_0$ is the excitation energy for $|\nu\rangle$ with \hbar being the Planck constant divided by 2π and E_0 being the energy of the ground state. On multiplying from the left by an arbitrary state $\langle G | \delta Q$, we have

$$\langle G | [\delta Q, [\mathcal{H}, Q_\nu^\dagger]] | G \rangle = \hbar\Omega_\nu \langle G | [\delta Q, Q_\nu^\dagger] | G \rangle. \quad (7)$$

In the RPA, electron correlation is considered in the ground state $|G\rangle$ [68,69]. Therefore, it consists of various states with multiple electrons and holes in addition to the ground state without the correlation $|g\rangle$, where one-particle states with energies below and above the Fermi energy are fully occupied and unoccupied, respectively. Low-lying excited states are assumed to be described by linear combinations of e-h pair states $a_m^\dagger b_i^\dagger |G\rangle$, where m and i denote states for an electron and hole, respectively, and a_m^\dagger and b_i^\dagger are creation operators of the states m and i , respectively. In addition, linear combinations of states given by $b_i a_m |G\rangle$, where an e-h pair is annihilated from the ground state, are considered. Thus, a creation operator Q_ν^\dagger is written as [68,69]

$$Q_\nu^\dagger = \sum_{m,i} X'_{mi} a_m^\dagger b_i^\dagger - \sum_{m',i'} Y'_{m'i'} b_{i'} a_{m'}, \quad (8)$$

where m' (i') denotes an electron (hole) state and X'_{mi} and $Y'_{m'i'}$ are expansion coefficients. When we choose δQ as $\delta Q = \{b_i a_m, a_m^\dagger b_i^\dagger\}$ in Eq. (7) for the excited states given by Eq. (8), we have the equations [68,69]

$$\langle G | [b_i a_m, [\mathcal{H}, Q_\nu^\dagger]] | G \rangle = \hbar\Omega_\nu \langle G | [b_i a_m, Q_\nu^\dagger] | G \rangle, \quad (9)$$

$$\langle G | [a_m^\dagger b_i^\dagger, [\mathcal{H}, Q_\nu^\dagger]] | G \rangle = \hbar\Omega_\nu \langle G | [a_m^\dagger b_i^\dagger, Q_\nu^\dagger] | G \rangle. \quad (10)$$

Substituting \mathcal{H} in Eq. (4) and Q_ν^\dagger in Eq. (8) into Eqs. (9) and (10) and assuming that $|G\rangle$ does not differ very much from $|g\rangle$ and $|G\rangle$ may be replaced by $|g\rangle$ in Eqs. (9) and (10), we have the RPA equation [68,69]

$$\begin{pmatrix} A' & B' \\ -B'^* & -A'^* \end{pmatrix} \begin{pmatrix} \mathbf{X}' \\ \mathbf{Y}' \end{pmatrix} = \hbar\Omega_\nu \begin{pmatrix} \mathbf{X}' \\ \mathbf{Y}' \end{pmatrix}, \quad (11)$$

with $(\mathbf{X}')_{mi} = X'_{mi}$, $(\mathbf{Y}')_{mi} = Y'_{mi}$, $A'_{mim'i'} = \delta_{m,m'} \delta_{i,i'} \epsilon_{mi} + \bar{v}_{(m;i)(i';m')}$, and $B'_{mim'i'} = \bar{v}_{(m;i)(m';i')}$, where ϵ_{mi} is the one-particle energy of an e-h pair state for an electron state m and hole one i , and

$$\bar{v}_{(r;t)(s;u)} = g_s v_{(r;t)(s;u)}^{(1)} + v_{(r;t)(s;u)}^{(2)}, \quad (12)$$

with $g_s = 2$ being the spin degeneracy and

$$v_{(r;t)(s;u)}^{(1)} = v_{(r;t)(s;u)}, \quad v_{(r;t)(s;u)}^{(2)} = -\frac{v_{(r;u)(s;t)}}{\epsilon(\mathbf{p}_r - \mathbf{p}_u)}, \quad (13)$$

where $\epsilon(\mathbf{p}_r - \mathbf{p}_u)$ is a static dielectric function and the wave vectors of holes are defined as those of the corresponding electron states. From Eq. (5), $v_{(r;t)(s;u)}^{(2)}$ vanishes for the valleys $v_r \neq v_u$ or $v_t \neq v_s$. The static dielectric function is given by [18]

$$\epsilon(\mathbf{p}_r - \mathbf{p}_u) = 1 + \frac{2e^2}{\kappa} I_{|\Delta|} \left(\frac{L|k_r - k_u|}{2\pi} \right) K_{|\Delta|} \left(\frac{L|k_r - k_u|}{2\pi} \right) \times [\Pi_\Delta^K(k_r - k_u) + \Pi_\Delta^{K'}(k_r - k_u)], \quad (14)$$

where $\Delta = (2\pi/L)^{-1}(\kappa_r - \kappa_u)$ is an integer because of $v_r = v_u$ and the static polarization function for electrons near the valley $v_r = v_u = \{K, K'\}$ becomes [18]

$$\Pi_\Delta^{v_r}(k_r - k_u) = -\frac{2}{A} \sum_{r',u'} \delta_{v_r, v_r'} \delta_{v_r, v_u'} \delta_{\Delta', \Delta} \delta_{k_r - k_u, k_r - k_u} \times |\mathbf{F}_u^\dagger \mathbf{F}_{r'}|^2 g_0(\epsilon_{r'}) g_0(\epsilon_{u'}) \frac{f_{r'} - f_{u'}}{\epsilon_{r'} - \epsilon_{u'}}, \quad (15)$$

with r' and u' being indices of one-particle states, $\Delta' = (2\pi/L)^{-1}(\kappa_{r'} - \kappa_{u'})$, $f_{r'}$ ($f_{u'}$) being the Fermi-Dirac distribution function for $\epsilon_{r'}$ ($\epsilon_{u'}$), and $g_0(\epsilon)$ being a cutoff function defined as $g_0(\epsilon) = \epsilon_c^{\alpha_c} / (|\epsilon|^{\alpha_c} + \epsilon_c^{\alpha_c})$, where ϵ_c is a cutoff energy and an exponent α_c is chosen such that $g_0(\epsilon)$ decays sufficiently fast. In the following, we consider 0 K in Eq. (15). In $v_{(r;t)(s;u)}^{(2)}$ in Eq. (13), the screening effects are necessary to be included for proper description of excited states as shown by Sham and Rice [70] and by many others for various systems [18,19,71–78]. In this study, we approximately use the above static dielectric function because it works well for energy bands of semiconducting and metallic nanotubes [79,80] and for excitons in nanotubes without doping [18,19]. The effects of the dynamical screening on the present system, which might especially modify excitons [81,82], remain as a future issue.

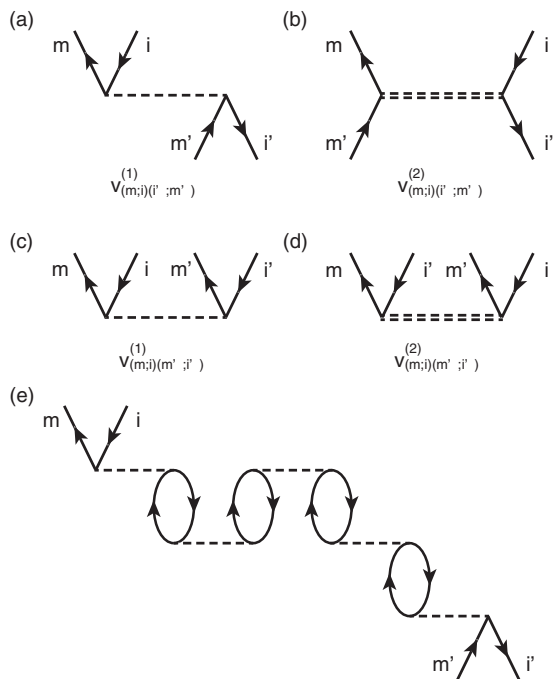


FIG. 1. Graphical representation of the matrix elements of the Coulomb interaction in the RPA equation. Panels (a) and (b) show $v_{(m;i)(i';m')}^{(1)}$ and $v_{(m;i)(i';m')}^{(2)}$, respectively, in A' and panels (c) and (d) show $v_{(m;i)(m';i')}^{(1)}$ and $v_{(m;i)(m';i')}^{(2)}$, respectively, in B' . Panel (e) shows an example of a part of the effective two-body interactions in the ring approximation. In panels (a), (c), and (e), dashed lines indicate the Coulomb interaction and in panels (b) and (d), double-dashed lines indicate the screened Coulomb interaction.

Figures 1(a)–1(d) show graphical representation of the matrix elements of the Coulomb interaction in A' and B' in the RPA equation (11). Graphical representation of those in A'^* and B'^* is given by the diagrams for A' and B' , respectively, which are placed upside down. The matrix elements in A' and A'^* denote processes where the numbers of electrons and holes do not change and those in B' (B'^*) indicate processes where the number of electrons and that of holes increase (decrease) by two. The matrix elements $v_{(r;t)(s;u)}^{(1)}$ describe depolarization effects and cause plasmons. In fact, connection of the diagrams for $v_{(r;t)(s;u)}^{(1)}$ leads to effective two-body interactions, which include the polarization of the medium, in the ring approximation in the calculation of the correlation energy [see Fig. 1(e)] [69]. The depolarization effects described by $v_{(r;t)(s;u)}^{(1)}$ in A' were discussed for cross-polarized excitons, excitons excited by cross-polarized light, in carbon nanotubes [20,83,84]. The matrix elements $v_{(r;t)(s;u)}^{(2)}$ in A' are attractive interactions, thus leading to excitons. It should be noted that in this study, the approximation in Eq. (11), which includes $v_{(r;t)(s;u)}^{(1)}$ and $v_{(r;t)(s;u)}^{(2)}$, is referred to as the RPA although the RPA usually means the approximation in Eq. (11) where $v_{(r;t)(s;u)}^{(2)}$ is eliminated.

In A' in Eq. (11), $v_{(m;i)(i';m')}^{(1)}$ indicates a part of the matrix elements of the Coulomb interaction between the basis states $a_m^\dagger b_i^\dagger |G\rangle$ and $a_{m'}^\dagger b_{i'}^\dagger |G\rangle$. From Eqs. (5) and (13), this is proportional to $(\mathbf{F}_m^\dagger \mathbf{F}_i)(\mathbf{F}_{i'}^\dagger \mathbf{F}_{m'})$. The factor $\mathbf{F}_m^\dagger \mathbf{F}_i$ is the matrix

element of the density operator between $a_m^\dagger b_i^\dagger |G\rangle$ and $|G\rangle$, where $|G\rangle$ is replaced by $|g\rangle$ in the calculation, and $\mathbf{F}_{i'}^\dagger \mathbf{F}_{m'}$ is the complex conjugate of that between $a_{m'}^\dagger b_{i'}^\dagger |G\rangle$ and $|G\rangle$. Thus, e-h pair states $a_m^\dagger b_i^\dagger |G\rangle$ for which $\mathbf{F}_m^\dagger \mathbf{F}_i$ does not vanish only contribute to the plasmons. The same applies for the basis states $b_i a_m |G\rangle$. Plasmons usually appear in energy above a one-particle excitation continuum or in energy gaps between continuums. Thus, we have two conditions for the existence of stable plasmons. One is that continuums have upper limits in energy and the other is that the matrix elements of the density operator for e-h pairs in the continuums are nonzero.

Since the wave vector of the ground state is assumed to be zero, the center-of-mass wave vectors of the basis states $a_m^\dagger b_i^\dagger |G\rangle$ and $b_i a_m |G\rangle$ are given by $\mathbf{p}_m - \mathbf{p}_i$ and $-\mathbf{p}_{m'} + \mathbf{p}_{i'}$, respectively. The center-of-mass wave vector is conserved in infinitely long carbon nanotubes and carbon nanotubes with periodic boundaries. In this case, excited states with a center-of-mass wave vector \mathbf{d} , which are denoted by $|v, \mathbf{d}\rangle$, are expanded by the basis states with the same center-of-mass wave vector $a_m^\dagger b_i^\dagger |G\rangle$ and $b_i a_m |G\rangle$, where $\mathbf{p}_m - \mathbf{p}_i = -\mathbf{p}_{m'} + \mathbf{p}_{i'} = \mathbf{d}$.

In the following, we consider intravalley excited states, where the electron and hole of each e-h pair belong to the same valley, because they contribute to optical absorption. The details of the RPA equation for doped carbon nanotubes are given in Appendix A. Since Eq. (11) is an eigenvalue equation for the non-Hermitian matrix, it is not guaranteed that the excitation energy is real. This is closely related to the stability of the ground state [68,69]. In the following numerical calculations, it was carefully confirmed that the ground states are stable.

Since the cutoff energy is given by the half of the π bandwidth, $\sim 3\gamma_0$, we have $\varepsilon_c(2\pi\gamma/L)^{-1} = \sqrt{3}L/\pi a$ [19]. Thus, for a typical nanotube diameter of 1.4 nm, $\varepsilon_c(2\pi\gamma/L)^{-1} \approx 10$. In numerical calculations, the component of the wave vector in the axis direction is discretized with the width $2\pi/A$, implying finite-length nanotubes with periodic boundaries. For example, $A/L = 100$ with $\varepsilon_c(2\pi\gamma/L)^{-1} = 10$ corresponds to $A \sim 450$ nm. For doped nanotubes, we only consider electron doping, i.e., $\varepsilon_F(2\pi\gamma/L)^{-1} > 0$ with ε_F being the Fermi energy because the e-h symmetry is not severely broken due to the higher-order corrections.

C. Dynamical conductivity

The optical absorption spectra of carbon nanotubes are given as follows [16,17]: For the μ component of an external electric field $E_\mu(\mathbf{p}, \omega)$, with $\mu = \{x, y\}$, \mathbf{p} being a wave vector, and ω being a frequency, an induced current $j_\mu(\mathbf{p}, \omega)$ is given by $j_\mu(\mathbf{p}, \omega) = \sigma_{\mu\mu}(\mathbf{p}, \omega) E_\mu(\mathbf{p}, \omega)$, where $\sigma_{\mu\mu}(\mathbf{p}, \omega)$ is the Fourier transform of the diagonal component of the dynamical conductivity tensor in the μ direction. Since optical absorption in a unit area is proportional to $\text{Re}[j_\mu(\mathbf{p}, \omega) E_\mu(\mathbf{p}, \omega)^*]$, $\text{Re}[\sigma_{\mu\mu}(\mathbf{p}, \omega)]$ characterizes optical absorption spectra. For parallel polarization, the electric field is along the nanotube-axis (y) direction and homogeneous on the nanotube surface. Thus, the absorption spectra are characterized by $\text{Re}[\sigma_{yy}(\mathbf{p}, \omega)]$ with $\mathbf{p} = (0, 0)$. For cross polarization, the electric field projected onto the nanotube surface is along the circumference (x) direction and has the wave vectors $(\pm 2\pi/L, \approx 0)$. Thus,

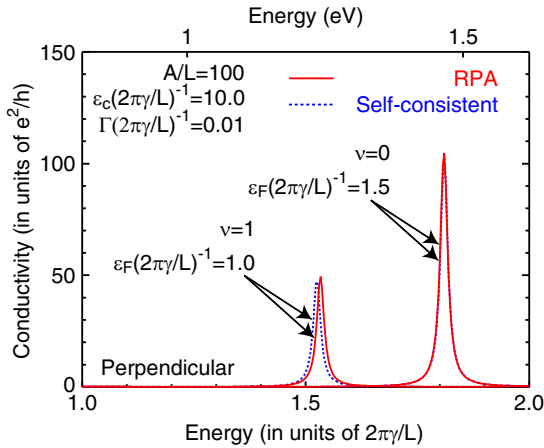


FIG. 2. Real part of the conductivity for cross polarization $\sigma_{xx}(\mathbf{p}, \omega)$ with $\mathbf{p} = (2\pi/L, 0)$, for metallic ($\nu = 0$) and semiconducting ($\nu = 1$) nanotubes with carrier doping in the lowest-order approximation. Solid and dotted lines denote results calculated in the RPA and with a self-consistent method [16,17] including exciton effects [20], respectively (see the main text). The Fermi energy is $\varepsilon_F(2\pi\gamma/L)^{-1} = 1.5$ for $\nu = 0$ and 1.0 for $\nu = 1$. $\varepsilon_c(2\pi\gamma/L)^{-1} = 10$ and $A/L = 100$.

optical absorption spectra are characterized by $\text{Re}[\sigma_{xx}(\mathbf{p}, \omega)]$ with $\mathbf{p} = (\pm 2\pi/L, 0)$. The dynamical conductivity is given from the Kubo formula by [85]

$$\sigma_{\mu\mu}(\mathbf{p}, \omega) = -\frac{ie^2 g_s}{\hbar AL} \sum_{\nu} \frac{2\omega |\langle \nu, \mathbf{p} | \hat{v}_{\mu, \mathbf{p}} | G \rangle|^2}{\Omega_{\nu}(\Omega_{\nu}^2 - \omega^2 - 2i\omega\Gamma/\hbar)}, \quad (16)$$

where $\hat{v}_{\mu, \mathbf{p}}$ is the μ component of the velocity operator with the wave vector \mathbf{p} , and Γ is phenomenological energy broadening. The detail of the calculations of the velocity matrix elements is given in Appendix B.

Since the excited states in the RPA include the depolarization effects as mentioned in Sec. II B, the dynamical conductivity calculated with these excited states describes the response not to the self-consistent electric field, which electrons actually feel, but to the external electric field. To illustrate this, in Fig. 2, we compare the dynamical conductivity calculated in the RPA with that calculated with another method [16,17,20] where the self-consistent electric field is calculated from the dynamical conductivity without the depolarization effects and then the conductivity with the depolarization effects is obtained from the self-consistent electric field. Peaks of the optical absorption spectra for doped metallic ($\nu = 0$) and semiconducting ($\nu = 1$) nanotubes come from cross-polarized plasmons. The results calculated with the two methods are in good agreement with each other. Slight deviation comes from the fact that the two methods are inequivalent because at least $v_{(m;i)(i';m')}^{(2)}$ and $v_{(m;i)(i';m')}^{(2)*}$ in B' and B'^* , respectively, in the RPA equation are not included in the other method.

Since the conductivities $\sigma_{xx}(\mathbf{p}, \omega)$ with $\mathbf{p} = (2\pi/L, k)$ and $(-2\pi/L, k)$, where k is the component in the nanotube-axis direction, are the same in our systems, results for $\mathbf{p} = (2\pi/L, k)$ are shown in the following. To detect the conductivity for finite k , it is needed to use nanotubes with short length [30] or

near fields localized in nanometer scale regions [86]. In the following numerical calculations, we choose $\Gamma(2\pi\gamma/L)^{-1} = 0.01$ as a typical value [87–91].

III. NUMERICAL RESULTS

In this section, results calculated in the lowest-order approximation are shown. In Fig. 3, the excitation energy of states with the center-of-mass wave vector $\mathbf{d} = (2\pi/L, q)$ with q being the component in the nanotube-axis direction is shown as a function of q . On the background, the real part of the dynamical conductivity $\sigma_{xx}(\mathbf{p}, \omega)$ with $\mathbf{p} = \mathbf{d}$ is shown. Figures 3(a), 3(c), and 3(e) show the results of metallic nanotubes and Figs. 3(b), 3(d), and 3(f) show those of semiconducting nanotubes with $\nu = 1$. Figures 3(a) and 3(b) are for no doping, Figs. 3(c) and 3(d) are for low-doping levels where the Fermi energy only crosses the lowest conduction band, and Figs. 3(e) and 3(f) are for high-doping levels where the Fermi energy reaches the second lowest conduction bands (see insets).

For metallic nanotubes in the no- and low-doping regimes in Figs. 3(a) and 3(c), continuums range from their lower boundaries to high energy without gaps. This is because the continuum in the high-energy region $\hbar\Omega_{\nu}(2\pi\gamma/L)^{-1} \gtrsim 1$, which arises from one-particle transitions between the valence band with $n = 0$ and the conduction band with $n = 1$, has large bandwidth and, in Fig. 3(c), it is connected to the continuum located in the lower energy $\hbar\Omega_{\nu}(2\pi\gamma/L)^{-1} \lesssim 1$ for transitions within the conduction bands. In this situation, plasmons are not expected to appear because they usually appear above continuums and decay in continuums. In fact, there are no dispersions of plasmons and no peak structures of the conductivity.

In Fig. 3(e) for the high-doping level, two gaps open at $q \sim 0$ above the two continuums for one-particle transitions in the conduction bands between $n = 1$ and 2 and between $n = 0$ and 1. The inset schematically shows the transitions. The continuum above the upper gap comes from transitions between the valence band with $n = 0$ and the conduction band with $n = 1$. The dispersion of a cross-polarized plasmon appears at $\hbar\Omega_{\nu}(2\pi\gamma/L)^{-1} \sim 1.8$ in the upper gap, along which the conductivity has large intensity. Thus, the plasmon energy is approximately given by the separation $\sim 2\pi\gamma/L$ between the conduction-band bottoms for $n = 1$ and 2 plus an energy shift due to the depolarization effects. When the Fermi energy is just above the bottom of the second lowest conduction band, the plasmon energy is $\sim 2\pi\gamma/L$ because the energy gap where the plasmon exists is closed at $\sim 2\pi\gamma/L$ by the lowering of the upper continuum.

A short energy dispersion for another cross-polarized plasmon exists at $\hbar\Omega_{\nu}(2\pi\gamma/L)^{-1} \approx 0.46$ in the lower gap as denoted by an arrow, for which the conductivity peak is small. This is because the lower-energy gap is narrow and the plasmon is suppressed by the upper continuum. This suppression could be understood in a similar way to that for cross-polarized excitons in carbon nanotubes [20]. When the energy of an excited state shifts upward due to the depolarization effects, the shifted energy is given by a zero point of the dielectric function describing the depolarization effects and the intensity of the peak of the optical absorption spectrum for the state is proportional to the inverse of the energy derivative of

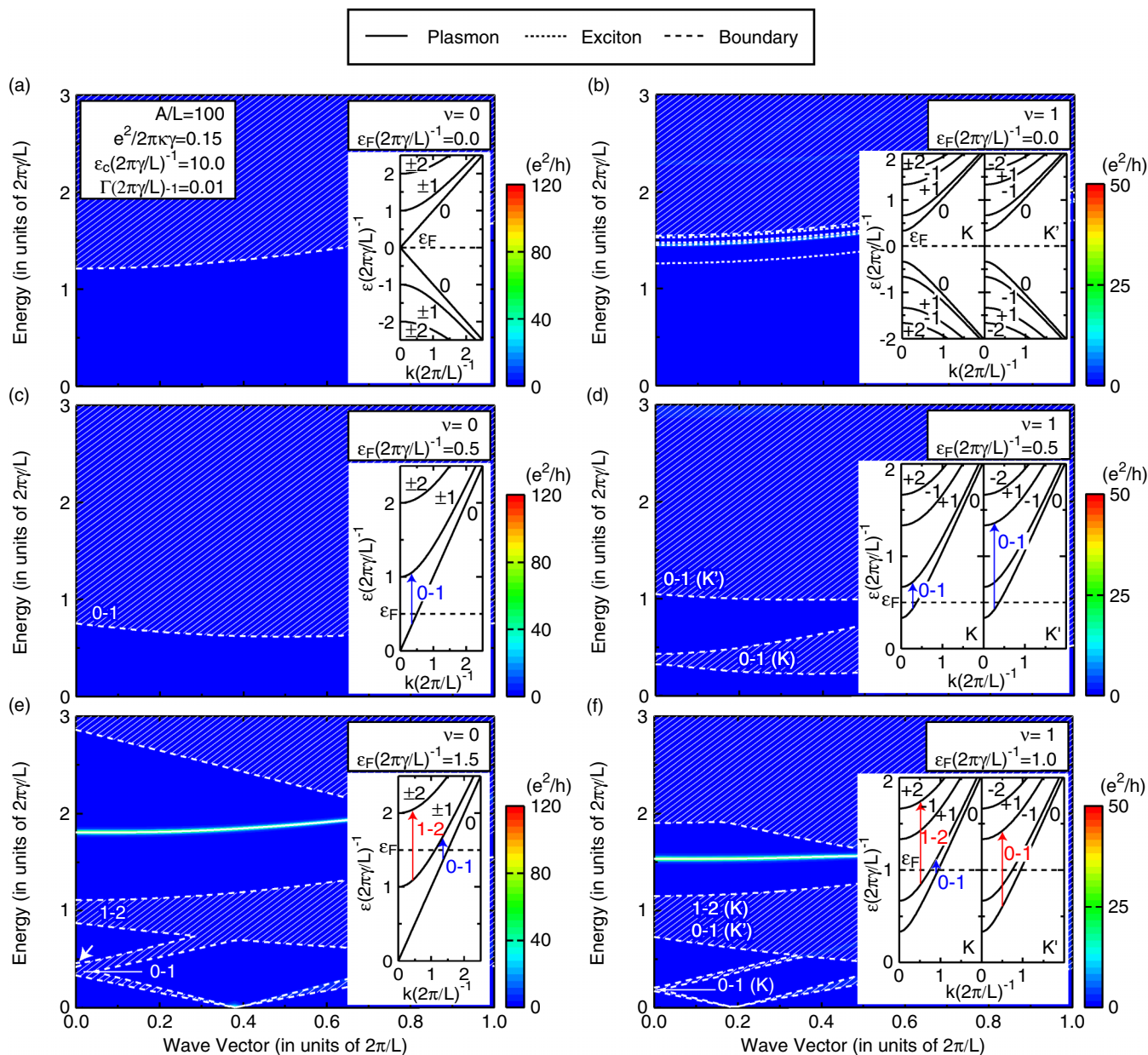


FIG. 3. Energy of excited states with the center-of-mass wave vector $\mathbf{d} = (2\pi/L, q)$ as a function of q in the lowest-order approximation. On the background, the real part of $\sigma_{xx}(\mathbf{p}, \omega)$ with $\mathbf{p} = \mathbf{d}$ is shown. Panels (a), (c), and (e) show results for metals and panels (b), (d), and (f) show those for semiconductors with $\nu = 1$. $\varepsilon_F(2\pi\gamma/L)^{-1} = 0$ in panels (a) and (b), 0.5 in panels (c) and (d), and 1.5 and 1.0 in panels (e) and (f), respectively. Solid and dotted lines denote the energy dispersions of plasmons and excitons, respectively. Hatched regions indicate continua and dashed lines are their boundaries. Characters $n-n'$ and $n-n'$ (ν) with n and n' being band indices and $\nu = \{K, K'\}$ specify continuums which come from transitions from the conduction band with $n = 0$ to that with n' (at the valley ν). $\varepsilon_c(2\pi\gamma/L)^{-1} = 10$ and $A/L = 100$. An arrow in panel (e) indicates the energy dispersion of a plasmon. Insets show the energy bands [at the K (left) and K' (right) points], where dashed lines denote the Fermi energy and arrows show one-particle transitions for the continua with $n-n'$ and $n-n'$ (ν).

the dielectric function at the energy. The dielectric function changes from minus infinity to plus infinity between two neighboring excitation energies without the depolarization effects. Thus, when an upper continuum is located near the plasmon energy, the energy shift is limited by the lower boundary of the continuum and the energy derivative of the dielectric function increases, leading to the suppression of the energy shift and the peak intensity for the excited state. This suppression will be explicitly demonstrated at the end of this section.

For nondoped semiconducting nanotubes in Fig. 3(b), there is no plasmon because of no energy gap above the continuum. There exist excitons, where optical transitions to the lowest and second lowest excitons are forbidden and allowed, respectively, and the latter is a bright cross-polarized exciton [20,45,47,92,93]. In Fig. 3(d) for the low-doping level, an energy gap opens at $q \sim 0$ above the continuum for transitions between the conduction bands with $n = 0$ and 1 at the K point. However, no plasmon exists in the gap. This is because for e-h pairs where electron states m and hole states i

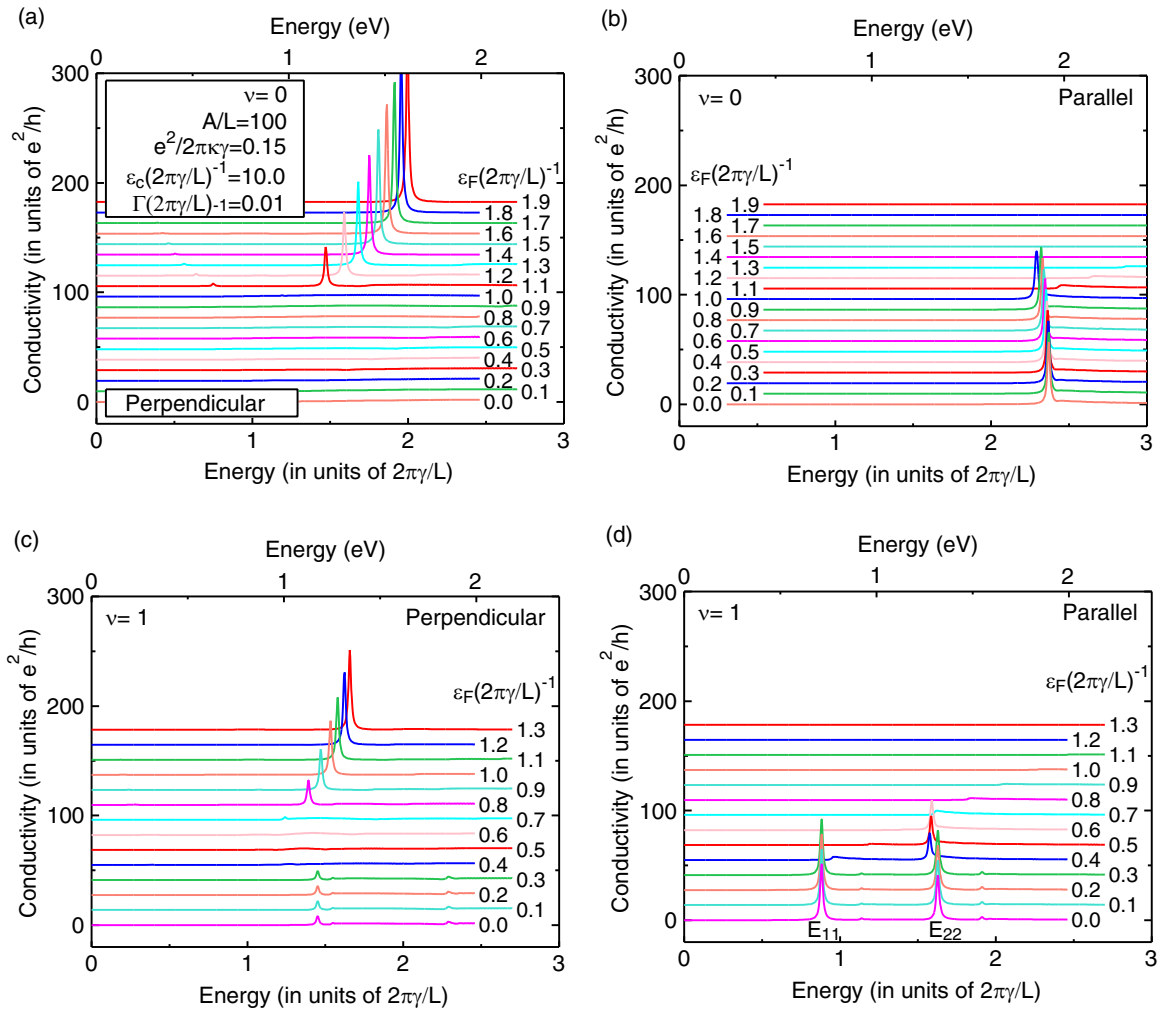


FIG. 4. Fermi-energy dependence of the real part of the conductivity for metallic nanotubes [(a) and (b)] and for semiconducting nanotubes with $\nu = 1$ [(c) and (d)] in the lowest-order approximation. Panels (a) and (c) show results for cross polarization and panels (b) and (d) show those for parallel polarization. The results with different values of the Fermi energy are vertically shifted for clarity. $\epsilon_c(2\pi\gamma/L)^{-1} = 10$ and $A/L = 100$.

are in the conduction bands with $n = 1$ and 0 , respectively, for the K point, $\mathbf{F}_m^\dagger \mathbf{F}_i$ is negligible for $|k_m|, |k_i| \ll 2\pi/L$ as can easily be shown from Eq. (3).

In Fig. 3(f) for the high-doping level, a plasmon appears in an energy gap above the continuum for transitions from $n = 1$ to 2 at the K point and from $n = 0$ to 1 at the K' point in the conduction bands. Therefore, the plasmon energy is approximately given by the separation $\sim 2\pi\gamma/L$ between the bottoms of these conduction bands with an energy shift due to the depolarization effects. For the Fermi energy just above the bottom of the second lowest conduction band, the plasmon energy is $\sim 2\pi\gamma/L$ because the gap where the plasmon exists closes at the energy by the lowering of the upper continuum. This is similar to the case of the metallic nanotubes. The energy dispersion of the plasmon was calculated with the classical electrodynamic theory by Wei and Wang [32]. In contrast to their result, the dispersion in our result is considerably small because of the suppression by the upper continuum in energy, which was mentioned above.

The Fermi-energy dependence of the conductivity for cross polarization, $\sigma_{xx}(\mathbf{p}, \omega)$ with $\mathbf{p} = (2\pi/L, 0)$, is shown for

metallic nanotubes in Fig. 4(a). Peaks arising from the plasmons appear when the Fermi energy reaches the second lowest bands $\epsilon_F(2\pi\gamma/L)^{-1} \gtrsim 1$ because of the opening of the energy gap above the continuum. With the increase of the Fermi energy, the plasmon energy and the peak intensity increase partly because the number of e-h pairs contributing to the plasmons increases and partly because the energy gap increases to decrease the suppression of the plasmon by the upper continuum. Slight peaks for $\hbar\Omega_\nu(2\pi\gamma/L)^{-1} \lesssim 0.8$ and $\epsilon_F(2\pi\gamma/L)^{-1} \gtrsim 1.1$ come from the plasmon associated with transitions between the conduction bands with $n = 0$ and 1 , which was shown in Fig. 3(e). The Fermi-energy dependence of the conductivity for parallel polarization, $\sigma_{yy}(\mathbf{p}, \omega)$ with $\mathbf{p} = (0, 0)$, is shown for metallic nanotubes in Fig. 4(b). Exciton peaks arise from transitions between the valence and conduction bands with $n = \pm 1$ in the no- and low-doping regimes, $\epsilon_F(2\pi\gamma/L)^{-1} \lesssim 1$ and disappear for $\epsilon_F(2\pi\gamma/L)^{-1} \gtrsim 1$ because the one-particle transitions associated with the excitons are partially blocked in the latter case. The appearance of the plasmon in Fig. 4(a) follows the disappearance of the exciton because the one-particle transitions associated with

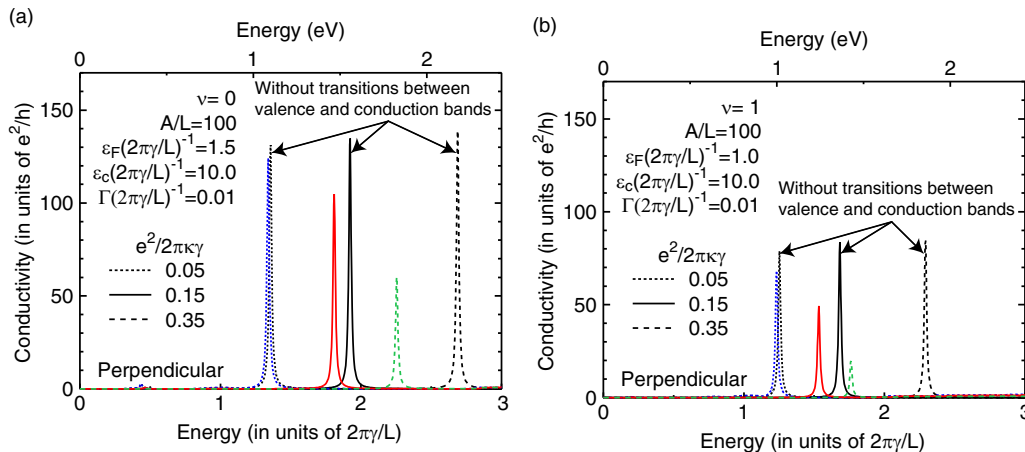


FIG. 5. Coulomb-interaction dependence of the real part of the conductivity for cross polarization for (a) metallic and (b) semiconducting ($\nu = 1$) nanotubes in the lowest-order approximation. $e^2/2\pi\kappa\gamma = 0.05$ (dotted lines), 0.15 (solid lines), and 0.35 (dashed lines). Results labeled “Without transitions between valence and conduction bands” are those calculated without continuums above the plasmon energies. In panels (a) and (b), $\varepsilon_F(2\pi\gamma/L)^{-1} = 1.5$ and 1.0, respectively. $\varepsilon_c(2\pi\gamma/L)^{-1} = 10$ and $A/L = 100$.

the excitons and the plasmons start to be blocked and occur, respectively, at the same time.

Figures 4(c) and 4(d) are similar plots for semiconducting nanotubes to Figs. 4(a) and 4(b), respectively. In Fig. 4(c), the plasmon appears for $\varepsilon_F(2\pi\gamma/L)^{-1} \gtrsim \frac{2}{3}$ because the Fermi energy reaches the second lowest conduction bands. For $\varepsilon_F(2\pi\gamma/L)^{-1} \lesssim \frac{2}{3}$, a cross-polarized exciton exists at $\hbar\Omega_v(2\pi\gamma/L)^{-1} \approx 1.45$ because associated one-particle transitions near the band bottoms occur. This energy is close to the plasmon energy at the Fermi energy where the plasmon starts to appear because the energies of the one-particle transitions associated with the plasmon and exciton are around $2\pi\gamma/L$. In Fig. 4(d), two exciton peaks appear, where the peaks at the lower and higher energies arise from the exciton ground states associated with one-particle transitions between the highest valence and the lowest conduction bands and between the second highest valence and the second lowest conduction bands, respectively. The former and latter are called E_{11} and E_{22} excitons, respectively. The peaks for the E_{11} and E_{22} excitons disappear for $\varepsilon_F(2\pi\gamma/L)^{-1} \gtrsim \frac{1}{3}$ and $\frac{2}{3}$, respectively, because the associated one-particle transitions are blocked. The appearance of the plasmon in Fig. 4(c) follows the disappearance of the E_{22} exciton because of the same reason as that for the metallic nanotubes.

The Coulomb-interaction dependence of the peaks of the conductivity arising from the cross-polarized plasmons is shown in Figs. 5(a) and 5(b) for metallic and semiconducting nanotubes, respectively, at typical doping levels. Results calculated without the continuums above the plasmon energies are also plotted. With the increase of the interactions, the plasmon energies increase and the peak intensities decrease in the results calculated with the continuums above the plasmon energies. This is because the increase of the Coulomb interaction enhances the upward shift of the plasmon energies due to the depolarization effects, leading to the increase of the interaction between the plasmons and the continuums above the plasmon energies, which suppresses the plasmons. In fact, when the continuums above the plasmon energies are absent, the energies and intensities for the peaks substantially increase

as compared to those calculated with the upper continuums, with the strength of the Coulomb interaction, indicating the validity of the explanation.

IV. DISCUSSIONS

We compare results calculated including the higher-order corrections with the experimental results [43]. In the experiments, the diameter of the used metallic nanotubes is about 1.4 nm, whose chiralities are not separated, and the used semiconducting nanotubes are (11, 10) and (6, 5) nanotube.

Figures 6(a) and 6(b) are the calculated Fermi-energy dependences of the conductivities for cross polarization and parallel polarization, respectively, for metallic (18, 0) nanotube with a diameter of about 1.4 nm. In Fig. 6(b), each calculated exciton peak splits into two because of the higher-order effects. An exciton peak in the experiments, whose position is shown by a dashed-dotted line, is single probably because the peak is an average over various chiralities. The experimental exciton energy reasonably agrees with the calculated ones although the former is slightly smaller than the average of the split exciton energies. This indicates that the parameters of our model are reasonable.

The unknown experimental Fermi energy can be estimated from plasmon peaks in Fig. 6(a). The calculated plasmon energies are slightly higher than the experimental one, where the deviation increases with the Fermi energy. Thus, the experimental Fermi energy is considered to be around that for the onset of the plasmon, $\varepsilon_F \sim 1$ eV, where the calculated plasmon energy is ~ 1.4 eV. The energy ~ 1.4 eV, is of the same order as but slightly larger than that calculated with the Drude conductivity, 1.027 eV, by Sasaki *et al.* [33]. The discrepancy is considered to arise partly from the chirality dependence of our results and partly from the difference between the models.

Figures 6(c)–6(f) are the conductivities for cross polarization [Figs. 6(c) and 6(e)] and parallel polarization [Figs. 6(d) and 6(f)] for semiconducting nanotubes, where Figs. 6(c) and 6(d) are results of (11, 10) nanotube and Figs. 6(e) and 6(f) are those of (6, 5) nanotube. For (11, 10) nanotube, the E_{11}

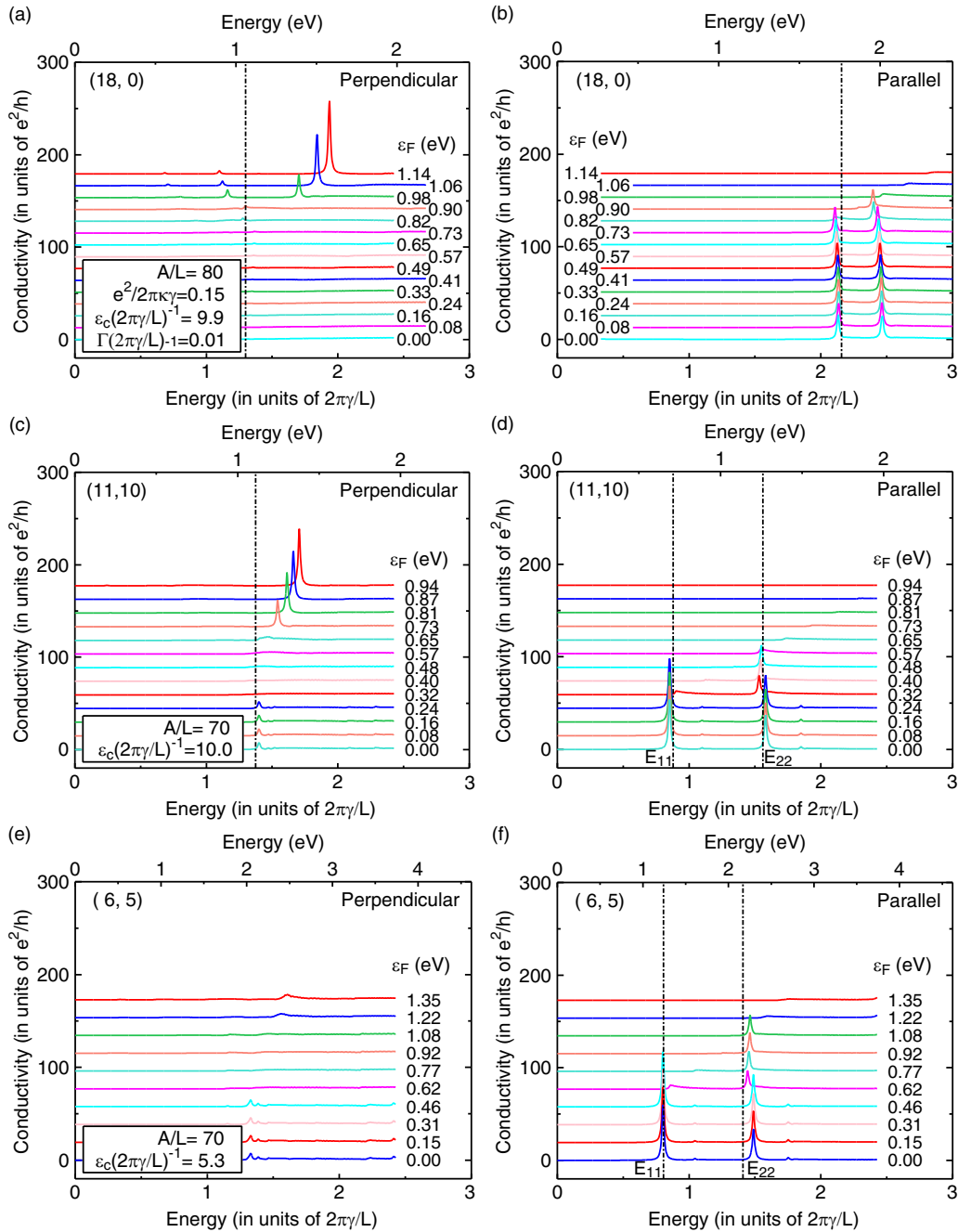


FIG. 6. Fermi-energy dependence of the real part of the conductivity with the higher-order corrections for (18, 0) metallic nanotube [(a) and (b)], and for (11, 10) [(c) and (d)] and (6, 5) [(e) and (f)] semiconducting nanotube. Panels (a), (c), and (e) show results for cross polarization and panels (b), (d), and (f) show those for parallel polarization. Vertical dashed-dotted lines in panels (a) and (c) indicate the experimental energies of cross-polarized plasmons and those in panels (b), (d), and (f) denote the experimental exciton energies [43]. In panels (a) and (b), $A/L = 80$ and in panels (c)–(f), $A/L = 70$.

and E_{22} exciton energies in Fig. 6(d) are in good agreement with the experimental ones. The experimental Fermi energy is estimated from the plasmon peaks in Fig. 6(c) in the same way as for the metallic nanotube and we have $\varepsilon_F \sim 0.7$ eV, where the plasmon energy is ~ 1.25 eV. For (6, 5) nanotube, the E_{11} and E_{22} exciton energies in Fig. 6(f) reasonably agree with the experimental results. Clear peaks for the plasmon do not appear for $\varepsilon_F \leq 1.35$ eV in Fig. 6(e) because the bottom of the second lowest conduction band for (6, 5) nanotube is higher than that for (11, 10) nanotube. In fact, the plasmon

peak appears for (11, 10) nanotube but not for (6, 5) nanotube in the experiments, suggesting the validity of our estimation of the Fermi energy.

V. SUMMARY AND CONCLUSIONS

In conclusion, we have numerically studied cross-polarized plasmons in doped carbon nanotubes in an effective-mass approximation and the random-phase approximation. For both metallic and semiconducting nanotubes, the cross-polarized

plasmons appear for high-doping level where the Fermi energy reaches the second lowest conduction band or the second highest valence band. In the Fermi-energy dependence of excited states, the appearance of the plasmons follows the disappearance of excitons. The excitation energy of the plasmons depends on the Fermi energy. For the Fermi energy just above the bottom of the second lowest conduction band or just below the top of the second highest valence band, the plasmon energy approximately becomes $2\pi\gamma/L$, which is typically of the order of one electron volt. Our results are in good agreement with recent experimental results.

APPENDIX A: RPA FOR DOPED CARBON NANOTUBES

For doped carbon nanotubes, excited states are expanded by four types of basis states $a_m^\dagger b_i^\dagger |G\rangle$ and $b_i a_m |G\rangle$ with $s_m = s_i$ and $a_m^\dagger b_i^\dagger |G\rangle$ and $b_i a_m |G\rangle$ with $s_m = -s_i$, where $s_m = \{\pm 1\}$ indicates the conduction (+1) and valence (-1) bands to which an electron state m belongs and s_i is that for a hole state i . Since the center-of-mass wave vector is conserved, all the basis states for excited states $|\nu, \mathbf{d}\rangle$, with a center-of-mass wave vector \mathbf{d} , have the same center-of-mass wave vector. We consider intravalley excited states, which contribute to optical absorption. Thus, creation operators Q_v^\dagger for the excited states are given by [54,68,69]

$$Q_v^\dagger = \sum_{m,i} \delta_{v_m, v_i} \left[\delta_{s_m, s_i} (\delta_{\mathbf{p}_m - \mathbf{p}_i, \mathbf{d}} U_{mi} a_m^\dagger b_i^\dagger - \delta_{\mathbf{p}_i - \mathbf{p}_m, \mathbf{d}} V_{mi} b_i a_m) + \delta_{s_m, -s_i} (\delta_{\mathbf{p}_m - \mathbf{p}_i, \mathbf{d}} X_{mi} a_m^\dagger b_i^\dagger - \delta_{\mathbf{p}_i - \mathbf{p}_m, \mathbf{d}} Y_{mi} b_i a_m) \right], \quad (\text{A1})$$

where v_m and v_i indicate the valleys to which an electron state m and hole one i , respectively, belong and U_{mi} , X_{mi} , V_{mi} , and Y_{mi} are expansion coefficients. In Eq. (A1), U_{mi} and V_{mi} are expansion coefficients for e-h pairs where electrons and holes belong to the conduction or valence band, and X_{mi} and Y_{mi} are those for e-h pairs where electrons and holes are in the conduction and valence bands, respectively. For each expansion coefficient, m is uniquely determined by i or vice versa.

The excited states with \mathbf{d} are separately determined from those with the other center-of-mass wave vectors. Calculating the matrix elements in the RPA equation in Eq. (11), the RPA equation for the excited states with \mathbf{d} in doped carbon nanotubes is given by [54,68,69]

$$\begin{array}{c} K \\ K' \\ K \\ K' \\ K \\ K' \\ K \end{array} \begin{pmatrix} KK' & KK' & K'K & K'K \\ A_{uu} & A_{ux} & B_{uv} & B_{uy} \\ A_{xu} & A_{xx} & B_{xv} & B_{xy} \\ -B_{uv} & -B_{uy} & -A_{uu} & -A_{ux} \\ -B_{xv} & -B_{xy} & -A_{xu} & -A_{xx} \end{pmatrix} \begin{pmatrix} \mathbf{U} \\ \mathbf{X} \\ \mathbf{V} \\ \mathbf{Y} \end{pmatrix} = \hbar\Omega_v \begin{pmatrix} \mathbf{U} \\ \mathbf{X} \\ \mathbf{V} \\ \mathbf{Y} \end{pmatrix}, \quad (\text{A2})$$

where $(\mathbf{U})_i = U_{mi}$, $(\mathbf{X})_i = X_{mi}$, $(\mathbf{V})_i = V_{mi}$, $(\mathbf{Y})_i = Y_{mi}$, and

$$(A_{uu})_{i,j} = \delta_{i,j} (\varepsilon_{s_i, \mathbf{p}_i + \mathbf{d}}^{v_i} - \varepsilon_{s_i, \mathbf{p}_i}^{v_i} + \Sigma_{s_i, \mathbf{p}_i + \mathbf{d}}^{v_i} - \Sigma_{s_i, \mathbf{p}_i}^{v_i}) + \bar{v}_{(s_i, \mathbf{p}_i + \mathbf{d}; s_i, \mathbf{p}_i)(s_j, \mathbf{p}_j; s_j, \mathbf{p}_j + \mathbf{d})}^{v_i v_i v_j v_j}, \quad (\text{A3})$$

$$(A_{ux})_{i,j} = \bar{v}_{(s_i, \mathbf{p}_i + \mathbf{d}; s_i, \mathbf{p}_i)(s_j, \mathbf{p}_j; -s_j, \mathbf{p}_j + \mathbf{d})}^{v_i v_i v_j v_j}, \quad (\text{A4})$$

$$(A_{xu})_{i,j} = \bar{v}_{(-s_i, \mathbf{p}_i + \mathbf{d}; s_i, \mathbf{p}_i)(s_j, \mathbf{p}_j; s_j, \mathbf{p}_j + \mathbf{d})}^{v_i v_i v_j v_j}, \quad (\text{A5})$$

$$(A_{xx})_{i,j} = \delta_{i,j} (\varepsilon_{-s_i, \mathbf{p}_i + \mathbf{d}}^{v_i} - \varepsilon_{-s_i, \mathbf{p}_i}^{v_i} + \Sigma_{-s_i, \mathbf{p}_i + \mathbf{d}}^{v_i} - \Sigma_{-s_i, \mathbf{p}_i}^{v_i}) + \bar{v}_{(-s_i, \mathbf{p}_i + \mathbf{d}; s_i, \mathbf{p}_i)(s_j, \mathbf{p}_j; -s_j, \mathbf{p}_j + \mathbf{d})}^{v_i v_i v_j v_j}, \quad (\text{A6})$$

$$(B_{uv})_{i,j} = \bar{v}_{(s_i, \mathbf{p}_i + \mathbf{d}; s_i, \mathbf{p}_i)(s_j, \mathbf{p}_j - \mathbf{d}; s_j, \mathbf{p}_j)}^{v_i v_i v_j v_j}, \quad (\text{A7})$$

$$(B_{uy})_{i,j} = \bar{v}_{(s_i, \mathbf{p}_i + \mathbf{d}; s_i, \mathbf{p}_i)(-s_j, \mathbf{p}_j - \mathbf{d}; s_j, \mathbf{p}_j)}^{v_i v_i v_j v_j}, \quad (\text{A8})$$

$$(B_{xv})_{i,j} = \bar{v}_{(-s_i, \mathbf{p}_i + \mathbf{d}; s_i, \mathbf{p}_i)(s_j, \mathbf{p}_j - \mathbf{d}; s_j, \mathbf{p}_j)}^{v_i v_i v_j v_j}, \quad (\text{A9})$$

$$(B_{xy})_{i,j} = \bar{v}_{(-s_i, \mathbf{p}_i + \mathbf{d}; s_i, \mathbf{p}_i)(-s_j, \mathbf{p}_j - \mathbf{d}; s_j, \mathbf{p}_j)}^{v_i v_i v_j v_j}, \quad (\text{A10})$$

with j being the index of a hole state,

$$\bar{v}_{(s_r, \mathbf{p}_r; s_r, \mathbf{p}_r)(s_s, \mathbf{p}_s; s_u, \mathbf{p}_u)}^{v_r v_r v_s v_s v_u v_u} = \bar{v}_{(r;t)(s;u)}, \quad (\text{A11})$$

and $\Sigma_{s_r, \mathbf{p}_r}^{v_r}$ being the self-energy given by [18]

$$\Sigma_{s_r, \mathbf{p}_r}^{v_r} = \sum_i v_{(r;r)(i;i)}^{(2)} g_c(\varepsilon_i), \quad (\text{A12})$$

where the cutoff function is introduced in the summation. In Eqs. (A3)–(A10), the subscripts i and j only indicate holes of e-h pairs with \mathbf{d} for the corresponding expansion coefficients. In Eq. (A2), we arrange the elements of \mathbf{U} , \mathbf{V} , \mathbf{X} , and \mathbf{Y} in such a way that the order of $V_{m'i'}$ at the K (K') point in \mathbf{V} is the same as that of U_{mi} at the K' (K) point in \mathbf{U} where $\mathbf{p}_m = -\mathbf{p}_{m'}$ and $\mathbf{p}_i = -\mathbf{p}_{i'}$ and the same is applied for \mathbf{Y} and \mathbf{X} . The matrix on the left-hand side of Eq. (A2) is a different form from that in Eq. (11) because the former is for the equation only for the basis states with \mathbf{d} . If the basis states with $-\mathbf{d}$ are included, the matrix becomes the same form as that in Eq. (11). Since Eq. (A2) is an eigenvalue equation for the non-Hermitian matrix, the orthonormalization condition for the eigenvectors for Eq. (A2) is different from that for the eigenvectors of Hermitian matrices [68,69]. The normalization condition is given by [68,69]

$$\sum_{(m,i)} |U_{mi}|^2 + \sum_{(m,i)} |X_{mi}|^2 - \sum_{(m,i)} |V_{mi}|^2 - \sum_{(m,i)} |Y_{mi}|^2 = 1, \quad (\text{A13})$$

where the summations run over possible e-h pairs for the corresponding expansion coefficients.

APPENDIX B: VELOCITY MATRIX ELEMENTS

The velocity operator for a wave vector \mathbf{p} is given by

$$\hat{v}_{\mu, \mathbf{p}} = \frac{1}{2} [v_\mu(\hat{\mathbf{k}}) e^{i\mathbf{p}\cdot\hat{\mathbf{r}}} + e^{i\mathbf{p}\cdot\hat{\mathbf{r}}} v_\mu(\hat{\mathbf{k}})], \quad (\text{B1})$$

where $\mu = \{x, y\}$, $\hat{\mathbf{r}} = (\hat{x}, \hat{y})$ is the position operator, and $v_\mu(\hat{\mathbf{k}}) = \hbar^{-1} \partial H / \partial \hat{k}_\mu$. For the K point, we have

$$v_\mu^K(\hat{\mathbf{k}}) = \frac{\gamma}{\hbar} \begin{pmatrix} \sqrt{3} a S \hat{k}_\mu & V_\mu(\hat{\mathbf{k}}) \\ V_\mu(\hat{\mathbf{k}})^\dagger & \sqrt{3} a S \hat{k}_\mu \end{pmatrix} \quad (\text{B2})$$

with

$$V_x(\hat{\mathbf{k}}) = 1 + \frac{\beta a}{2\sqrt{3}} e^{3i\eta} (\hat{k}_x + i\hat{k}_y), \quad (\text{B3})$$

$$V_y(\hat{\mathbf{k}}) = -i + \frac{i\beta a}{2\sqrt{3}} e^{3i\eta} (\hat{k}_x + i\hat{k}_y). \quad (\text{B4})$$

The velocity operator for the K' point is obtained in the same way. Assuming that $|G\rangle$ does not differ very much from $|g\rangle$, velocity matrix elements between the excited states $|\nu, \mathbf{d}\rangle$ and

the ground state $|G\rangle$ are given by [54,68,69]

$$\begin{aligned} \langle \nu, \mathbf{d} | \hat{v}_{\mu, \mathbf{d}} | G \rangle &= \sum_{\langle m, i \rangle} U_{mi}^* (v_{\mu, \mathbf{d}})_{mi} + \sum_{\langle m, i \rangle} V_{mi}^* (v_{\mu, \mathbf{d}})_{im} \\ &+ \sum_{\langle m, i \rangle} X_{mi}^* (v_{\mu, \mathbf{d}})_{mi} + \sum_{\langle m, i \rangle} Y_{mi}^* (v_{\mu, \mathbf{d}})_{im}, \end{aligned} \quad (\text{B5})$$

where $(v_{\mu, \mathbf{d}})_{rs} = \mathbf{F}_r^\dagger v_\mu^{rs} (\mathbf{p}_s + \mathbf{d}/2) \mathbf{F}_s$ and $|G\rangle$ is replaced by $|g\rangle$ in the calculation.

-
- [1] F. Stern, *Phys. Rev. Lett.* **18**, 546 (1967).
 [2] S. Das Sarma and W.-Y. Lai, *Phys. Rev. B* **32**, 1401 (1985).
 [3] T. Nagao, S. Yaginuma, T. Inaoka, and T. Sakurai, *Phys. Rev. Lett.* **97**, 116802 (2006).
 [4] T. Nagao, S. Yaginuma, T. Inaoka, T. Sakurai, and D. Jeon, *J. Phys. Soc. Jpn.* **76**, 114714 (2007).
 [5] C. Liu, T. Inaoka, S. Yaginuma, T. Nakayama, M. Aono, and T. Nagao, *Phys. Rev. B* **77**, 205415 (2008).
 [6] E. P. Rugeramigabo, C. Tegenkamp, H. Pfnür, T. Inaoka, and T. Nagao, *Phys. Rev. B* **81**, 165407 (2010).
 [7] T. Block, C. Tegenkamp, J. Baringhaus, H. Pfnür, and T. Inaoka, *Phys. Rev. B* **84**, 205402 (2011).
 [8] T. Lichtenstein, C. Tegenkamp, and H. Pfnür, *J. Phys.: Condens. Matter* **28**, 354001 (2016).
 [9] B. Wunsch, T. Stauber, F. Sols, and F. Guinea, *New J. Phys.* **8**, 318 (2006).
 [10] X.-F. Wang and T. Chakraborty, *Phys. Rev. B* **75**, 033408 (2007).
 [11] E. H. Hwang and S. Das Sarma, *Phys. Rev. B* **75**, 205418 (2007).
 [12] Y. Liu, R. F. Willis, K. V. Emtsev, and Th. Seyller, *Phys. Rev. B* **78**, 201403(R) (2008).
 [13] N. Kumada, S. Tanabe, H. Hibino, H. Kamata, M. Hashisaka, K. Muraki, and T. Fujisawa, *Nat. Commun.* **4**, 1363 (2013).
 [14] N. Kumada, R. Dubourget, K. Sasaki, S. Tanabe, H. Hibino, H. Kamata, M. Hashisaka, K. Muraki, and T. Fujisawa, *New J. Phys.* **16**, 063055 (2014).
 [15] K. I. Sasaki and N. Kumada, *Phys. Rev. B* **90**, 035449 (2014).
 [16] H. Ajiki and T. Ando, *Phys. B (Amsterdam)* **201**, 349 (1994).
 [17] H. Ajiki and T. Ando, *Jpn. J. Appl. Phys.* **34** (Suppl. 34-1), 107 (1995).
 [18] T. Ando, *J. Phys. Soc. Jpn.* **66**, 1066 (1997).
 [19] T. Ando, *J. Phys. Soc. Jpn.* **73**, 3351 (2004).
 [20] S. Uryu and T. Ando, *Phys. Rev. B* **74**, 155411 (2006).
 [21] Y. Wang, K. Kempa, B. Kimball, J. B. Carlson, G. Benham, W. Z. Li, T. Kempa, J. Rybczynski, A. Herczynski, and Z. F. Ren, *Appl. Phys. Lett.* **85**, 2607 (2004).
 [22] N. Akima, Y. Iwasa, S. Brown, A. M. Barbour, J. Cao, J. L. Musfeldt, H. Matsui, N. Toyota, M. Shiraishi, H. Shimoda, and O. Zhou, *Adv. Mater.* **18**, 1166 (2006).
 [23] M. Ichida, S. Saito, T. Nakano, Y. Feng, Y. Miyata, K. Yanagi, H. Kataura, and H. Ando, *Solid State Commun.* **151**, 1696 (2011).
 [24] M. V. Shuba, A. G. Paddubskaya, A. O. Plyushch, P. P. Kuzhir, G. Ya. Slepyan, S. A. Maksimenko, V. K. Ksenevich, P. Buka, D. Seliuta, I. Kasalynas *et al.*, *Phys. Rev. B* **85**, 165435 (2012).
 [25] Q. Zhang, E. H. Hároz, Z. Jin, L. Ren, X. Wang, R. S. Arvidson, A. Lüttge, and J. Kono, *Nano Lett.* **13**, 5991 (2013).
 [26] L. Ren, Q. Zhang, C. L. Pint, A. K. Wójcik, M. Bunney Jr., T. Arikawa, I. Kawayama, M. Tonouchi, R. H. Hauge, A. A. Belyanin, and J. Kono, *Phys. Rev. B* **87**, 161401(R) (2013).
 [27] T. Morimoto, S.-K. Joung, T. Saito, D. N. Futaba, K. Hata, and T. Okazaki, *ACS Nano* **8**, 9897 (2014).
 [28] G. Ya. Slepyan, S. A. Maksimenko, A. Lakhtakia, O. Yevtushenko, and A. V. Gusakov, *Phys. Rev. B* **60**, 17136 (1999).
 [29] J. Hao and G. W. Hanson, *Phys. Rev. B* **74**, 035119 (2006).
 [30] T. Nakanishi and T. Ando, *J. Phys. Soc. Jpn.* **78**, 114708 (2009).
 [31] G. Ya. Slepyan, M. V. Shuba, S. A. Maksimenko, C. Thomsen, and A. Lakhtakia, *Phys. Rev. B* **81**, 205423 (2010).
 [32] L. Wei and Y.-N. Wang, *Phys. Lett. A* **333**, 303 (2004).
 [33] K. Sasaki, S. Murakami, and H. Yamamoto, *Appl. Phys. Lett.* **108**, 163109 (2016).
 [34] A. Ugawa, A. G. Rinzler, and D. B. Tanner, *Phys. Rev. B* **60**, R11305 (1999).
 [35] M. E. Itkis, S. Niyogi, M. E. Meng, M. A. Hamon, H. Hu, and R. C. Haddon, *Nano Lett.* **2**, 155 (2002).
 [36] T.-I. Jeon, K.-J. Kim, C. Kang, S.-J. Oh, J.-H. Son, K. H. An, D. J. Bae, and Y. H. Lee, *Appl. Phys. Lett.* **80**, 3403 (2002).
 [37] F. Borondics, K. Kamarás, M. Nikolou, D. B. Tanner, Z. H. Chen, and A. G. Rinzler, *Phys. Rev. B* **74**, 045431 (2006).
 [38] T. Kampfrath, K. von Volkman, C. M. Aguirre, P. Desjardins, R. Martel, M. Krenz, C. Frischkorn, M. Wolf, and L. Perfetti, *Phys. Rev. Lett.* **101**, 267403 (2008).
 [39] Á. Pekker and K. Kamarás, *Phys. Rev. B* **84**, 075475 (2011).
 [40] R. R. Hartmann, I. A. Shelykh, and M. E. Portnoi, *Phys. Rev. B* **84**, 035437 (2011).
 [41] S. Kazaoui, N. Minami, N. Matsuda, H. Kataura, and Y. Achiba, *Appl. Phys. Lett.* **78**, 3433 (2001).
 [42] K. Yanagi, R. Moriya, N. T. Cuong, M. Otani, and S. Okada, *Phys. Rev. Lett.* **110**, 086801 (2013).
 [43] T. Igarashi, H. Kawai, K. Yanagi, N. T. Cuong, S. Okada, and T. Pichler, *Phys. Rev. Lett.* **114**, 176807 (2015).
 [44] C. D. Spataru, S. Ismail-Beigi, L. X. Benedict, and S. G. Louie, *Phys. Rev. Lett.* **92**, 077402 (2004).
 [45] E. Chang, G. Bussi, A. Ruini, and E. Molinari, *Phys. Rev. Lett.* **92**, 196401 (2004).
 [46] V. Perebeinos, J. Tersoff, and P. Avouris, *Phys. Rev. Lett.* **92**, 257402 (2004).
 [47] H. Zhao and S. Mazumdar, *Phys. Rev. Lett.* **93**, 157402 (2004).

- [48] C. L. Kane and E. J. Mele, *Phys. Rev. Lett.* **93**, 197402 (2004).
- [49] M. Ichida, S. Mizuno, Y. Tani, Y. Saito, and A. Nakamura, *J. Phys. Soc. Jpn.* **68**, 3131 (1999).
- [50] S. M. Bachilo, M. S. Strano, C. Kittrell, R. H. Hauge, R. E. Smalley, and R. B. Weisman, *Science* **298**, 2361 (2002).
- [51] F. Wang, G. Dukovic, L. E. Brus, and T. F. Heinz, *Science* **308**, 838 (2005).
- [52] F. Wang, D. J. Cho, B. Kessler, J. Deslippe, P. J. Schuck, S. G. Louie, A. Zettl, T. F. Heinz, and Y. R. Shen, *Phys. Rev. Lett.* **99**, 227401 (2007).
- [53] S. Uryu and T. Ando, *Phys. Rev. B* **77**, 205407 (2008).
- [54] S. Uryu, *Phys. Rev. B* **94**, 155451 (2016); **96**, 199906(E) (2017).
- [55] J. C. Slonczewski and P. R. Weiss, *Phys. Rev.* **109**, 272 (1958).
- [56] H. Ajiki and T. Ando, *J. Phys. Soc. Jpn.* **62**, 1255 (1993).
- [57] H. Ajiki and T. Ando, *J. Phys. Soc. Jpn.* **65**, 505 (1996).
- [58] T. Ando, *J. Phys. Soc. Jpn.* **74**, 777 (2005).
- [59] T. Ando, *J. Phys. Soc. Jpn.* **78**, 104703 (2009).
- [60] C. L. Kane and E. J. Mele, *Phys. Rev. Lett.* **78**, 1932 (1997).
- [61] C. L. Kane, E. J. Mele, R. S. Lee, J. E. Fischer, P. Petit, H. Dai, A. Thess, R. E. Smalley, A. R. M. Verschueren, S. J. Tans, and C. Dekker, *Europhys. Lett.* **41**, 683 (1998).
- [62] T. Ando, *J. Phys. Soc. Jpn.* **69**, 1757 (2000).
- [63] H. Suzuura and T. Ando, *Phys. E (Amsterdam)* **6**, 864 (2000).
- [64] H. Suzuura and T. Ando, *Mol. Cryst. Liq. Cryst.* **340**, 731 (2000).
- [65] H. Suzuura and T. Ando, *Phys. Rev. B* **65**, 235412 (2002).
- [66] S. Uryu, H. Ajiki, and T. Ando, *Phys. Rev. B* **78**, 115414 (2008).
- [67] S. Uryu and T. Ando, *Phys. Rev. B* **83**, 085404 (2011).
- [68] P. Ring and P. Schuck, *The Nuclear Many-Body Problem* (Springer, New York, 1980) and references therein.
- [69] A. Fetter and J. D. Walecka, *Quantum Theory of Many Particle Systems* (Dover, New York, 2003) and references therein.
- [70] L. J. Sham and T. M. Rice, *Phys. Rev.* **144**, 708 (1966).
- [71] R. Zimmermann, *Phys. Status Solidi B* **48**, 603 (1971).
- [72] G. Strinati, *Phys. Rev. Lett.* **49**, 1519 (1982).
- [73] G. Strinati, *Phys. Rev. B* **29**, 5718 (1984).
- [74] G. Onida, L. Reining, R. W. Godby, R. Del Sole, and W. Andreoni, *Phys. Rev. Lett.* **75**, 818 (1995).
- [75] S. Albrecht, G. Onida, and L. Reining, *Phys. Rev. B* **55**, 10278 (1997).
- [76] M. Rohlfing and S. G. Louie, *Phys. Rev. Lett.* **80**, 3320 (1998).
- [77] M. Rohlfing and S. G. Louie, *Phys. Rev. B* **62**, 4927 (2000).
- [78] L. X. Benedict, E. L. Shirley, and R. B. Bohn, *Phys. Rev. Lett.* **80**, 4514 (1998).
- [79] H. Sakai, H. Suzuura, and T. Ando, *J. Phys. Soc. Jpn.* **72**, 1698 (2003).
- [80] H. Sakai, H. Suzuura, and T. Ando, *Phys. E (Amsterdam)* **22**, 704 (2004).
- [81] C. D. Spataru and F. Léonard, *Phys. Rev. Lett.* **104**, 177402 (2010).
- [82] Y. Tomio and H. Suzuura, *JPS Conf. Proc.* **4**, 012006 (2015).
- [83] S. Uryu and T. Ando, *J. Phys.: Conf. Ser.* **302**, 012004 (2011).
- [84] H. Ajiki, *J. Phys. Soc. Jpn.* **82**, 054701 (2013).
- [85] R. Kubo, *J. Phys. Soc. Jpn.* **12**, 570 (1957).
- [86] S. Uryu, H. Ajiki, and H. Ishihara, *Phys. Rev. Lett.* **110**, 257401 (2013).
- [87] M. W. Graham, Y.-Z. Ma, A. A. Green, M. C. Hersam, and G. R. Fleming, *J. Chem. Phys.* **134**, 034504 (2011).
- [88] K. Matsuda, T. Inoue, Y. Murakami, S. Maruyama, and Y. Kanemitsu, *Phys. Rev. B* **77**, 033406 (2008).
- [89] K. Yoshikawa, R. Matsunaga, K. Matsuda, and Y. Kanemitsu, *Appl. Phys. Lett.* **94**, 093109 (2009).
- [90] D. T. Nguyen, C. Voisin, Ph. Roussignol, C. Roquelet, J. S. Lauret, and G. Cassabois, *Phys. Rev. B* **84**, 115463 (2011).
- [91] Y. Fujimoto and S. Uryu, *Phys. Rev. B* **88**, 235408 (2013).
- [92] Y. Miyauchi, M. Oba, and S. Maruyama, *Phys. Rev. B* **74**, 205440 (2006).
- [93] J. Lefebvre and P. Finnie, *Phys. Rev. Lett.* **98**, 167406 (2007).